

Planar hyperlens based on a modulated graphene monolayer

Ebrahim Forati and George W. Hanson*

Department of Electrical Engineering, University of Wisconsin-Milwaukee, 3200 N. Cramer St., Milwaukee, Wisconsin 53211, USA

Alexander B. Yakovlev

Center for Applied Electromagnetic Systems Research (CAESR), Department of Electrical Engineering, University of Mississippi, University, Mississippi 38677-1848, USA

Andrea Alù

Department of Electrical and Computer Engineering, University of Texas at Austin, Austin, Texas 78712, USA

(Received 10 December 2013; revised manuscript received 24 January 2014; published 28 February 2014)

The canalization of terahertz surface plasmon polaritons using a modulated graphene monolayer is investigated for subwavelength imaging. An anisotropic surface conductivity formed by a set of parallel nanoribbons with alternating positive and negative imaginary conductivities is used to realize the canalization regime required for hyperlensing. The ribbons are narrow compared to the wavelength and are created electronically by gating a graphene layer over a corrugated ground plane. Good quality canalization of surface plasmon polaritons is shown in the terahertz even in the presence of realistic loss in graphene, with relevant implications for subwavelength imaging applications.

DOI: [10.1103/PhysRevB.89.081410](https://doi.org/10.1103/PhysRevB.89.081410)

PACS number(s): 73.20.Mf, 81.05.Xj, 78.67.Wj

I. INTRODUCTION

Graphene, the first 2D material to be practically realized [1], has attracted great interest in the last decade. The fact that electrons in graphene behave as massless Dirac fermions leads to a variety of anomalous properties [2,3], such as charge carriers with ultra-high-mobility and long mean-free paths, gate-tunable carrier densities, and anomalous quantum Hall effects [4]. Graphene's electrical properties have been studied in many previous works [5–14] and are often represented by a local complex surface conductivity given by the Kubo formula [15,16]. Since its surface conductivity leads to attractive surface plasmon properties, graphene has become a good candidate for plasmonic applications, especially in the terahertz (THz) regime [17–25].

Surface plasmons (SPs) are the collective charge oscillations at the surface of plasmonic materials. SPs coupled with photons form the composite quasiparticles known as surface plasmon polaritons (SPPs). Theoretically, the dispersion relationship for SPPs on a surface can be obtained as a solution of Maxwell's equations [26]. In this approach, it is easy to show that, in order to support the SPP, 3D materials with negative bulk permittivities (e.g., noble metals) or 2D materials with nonzero imaginary surface conductivities (e.g., graphene) are essential. Although SPPs on metals and on graphene have considerable qualitative similarities, graphene SPPs generally exhibit stronger confinement to the surface, efficient wave localization up to mid-infrared frequencies [19,27], and they are highly tunable (which is one of their most unique and important properties) [3]. Applications of graphene SPPs include electronics [28–30], optics [31–33], THz technology [34–36], light harvesting [37], metamaterials [38], and medical sciences [39,40]. In this work, we study the canalization of SPPs on graphene, which can

have direct applications for subwavelength imaging using THz sources.

Subwavelength imaging using metamaterials was first reported by Pendry in 2000 [41]. His technique [42] was based on backward waves, negative refraction, and amplification of evanescent waves. More recently, another more robust venue for subwavelength imaging was proposed, based on metamaterials operating in the so-called “canalization regime” [43–45]. In this case, the structure (acting as a transmission medium) transfers subwavelength images from a source plane to an image plane over distances of several wavelengths, without diffraction [46]. This form of super-resolving imaging, or hyperlensing, can also be realized by a uniaxial wire medium [47]. In these schemes, all spatial harmonics (evanescent and propagating) propagate with the same phase velocity from the near to the far field. In this Rapid Communication, we discuss the canalization of SPPs on a modulated graphene monolayer. In Ref. [48], it was shown that the near field of a vertical point source placed in close proximity to a graphene monolayer couples primarily to the field of an SPP strongly confined to the monolayer. By creating an anisotropic graphene surface as alternating graphene nanoribbons with positive and negative imaginary surface conductivities, we achieve SPP canalization and hyperlensing of the near field of an arbitrary source.

To achieve canalization, it is necessary to realize a flat isofrequency contour [49]. Here, taking the same definition for canalization as for a 3D material, we first study the conditions for canalization of SPPs on a 2D material such as graphene. Then, a practical geometry is proposed and verified for the hyperlens implementation.

II. THEORY AND FORMULATION

Figure 1 shows an infinite graphene layer in the yz plane suspended in vacuum. Its surface conductivity is assumed isotropic (σ_0) everywhere except in the region between

*george@uwm.edu

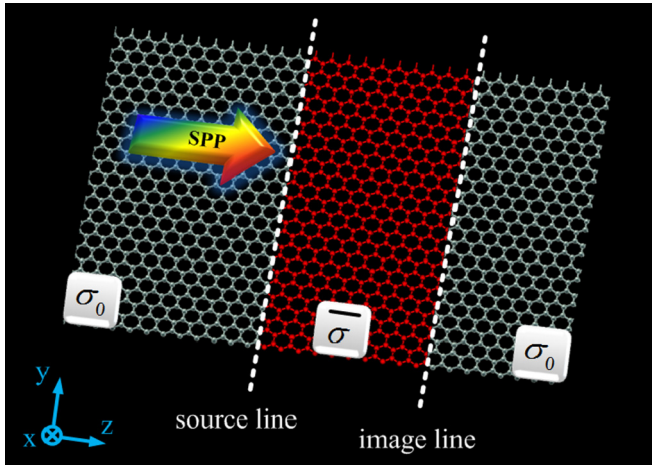


FIG. 1. (Color online) An infinite graphene layer in the yz plane. The conductivity of graphene is isotropic (σ_0) everywhere except in the red region, where it is anisotropic ($\bar{\sigma}$). The anisotropic region will be created by a suitable gate bias.

the source and image lines (red colored region), which is anisotropic and is given as

$$\bar{\sigma} = \sigma_y \hat{y}\hat{y} + \sigma_z \hat{z}\hat{z} = -j(\sigma_y^i \hat{y}\hat{y} + \sigma_z^i \hat{z}\hat{z}), \quad (1)$$

where for now $\sigma_{y,z}$ are assumed to be imaginary-valued, (to be generalized later) $\sigma_{y,z} = 0 - j\sigma_{y,z}^i$. For an SPP traveling over such an anisotropic graphene layer, it is possible [50] to show that the governing dispersion relation is

$$\begin{aligned} k_z^2 \left(\frac{\sigma_z^i}{\sigma_z^i + \sigma_y^i} \right) + k_y^2 \left(\frac{\sigma_y^i}{\sigma_z^i + \sigma_y^i} \right) - k_0^2 \\ = \frac{k_0 k_x}{\sigma_z^i + \sigma_y^i} \left(\frac{2}{\eta_0} - \frac{\eta_0 \sigma_y^i \sigma_z^i}{2} \right), \end{aligned} \quad (2)$$

where k_0 is the wave number in free space, $\eta_0 = \sqrt{\mu_0/\epsilon_0}$ is the intrinsic impedance of vacuum, $k_x = \sqrt{k_y^2 + k_z^2 - k_0^2}$, and the 2D spatial Fourier transform variables are $(y, z) = (k_y, k_z)$.

From (2), an ideal canalization regime can be realized when

$$\sigma_y^i \rightarrow 0; \quad \sigma_z^i \rightarrow \infty, \quad (3)$$

simultaneously, such that (2) becomes

$$k_z = k_0, \quad (4)$$

independent of k_y . Equation (4) implies that all of the transverse spatial harmonics (k_y of the SPPs) will propagate with the same wave number (phase velocity) in the z direction. In this situation, which is analogous to the canalization regime in 3D metamaterials, any SPP distribution at the source line in Fig. 1 will be transferred to the image line without diffraction or any phase distortion. Condition (3) is somewhat analogous to the condition required for canalization of 3D waves in Ref. [51], but with the difference that here the extreme parameters (3) yield a finite wave number, equal to the background medium surrounding the modulated graphene layer, and not zero as for the 3D case. This is to be expected, since the canalized SPPs still need to be above the light cone to avoid radiation and leakage in the background medium.

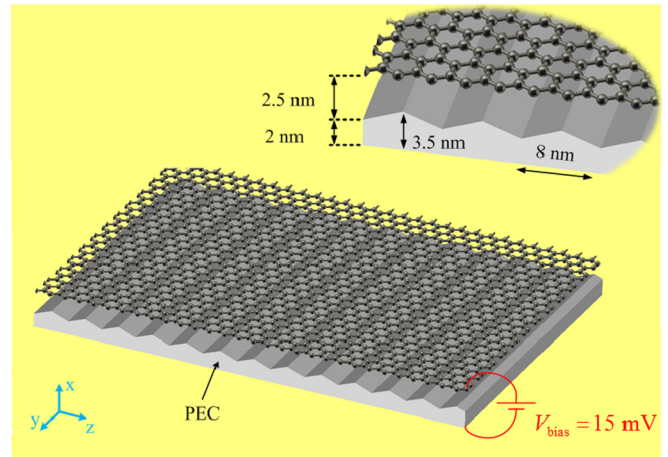


FIG. 2. (Color online) Triangular ridged ground plane for achieving conductivity modulation (leading to a soft-boundary profile).

Quite peculiarly, it follows from (4) that the confinement in the transverse (x) direction of each SPP is proportional to its spatial frequency along y , i.e., $k_x = k_y$.

It might seem difficult to find a natural 2D material providing (3) for canalization. However, it can be shown [50] that a modulated isotropic conductivity $\sigma(z)$ can act as an effective anisotropic conductivity,

$$\sigma_y^{\text{eff}} = \frac{1}{T} \int_{(T)} \sigma(z) dz, \quad (5)$$

$$\frac{1}{\sigma_z^{\text{eff}}} = \frac{1}{T} \int_{(T)} \frac{1}{\sigma(z)} dz, \quad (6)$$

where $\sigma(z)$ is assumed to be periodic with period T , and the integrations are over one period. Note that T should be small compared to the wavelength in order to provide valid effective parameters. Therefore, if the isotropic conductivity of graphene is properly modulated (e.g., by electrical gating

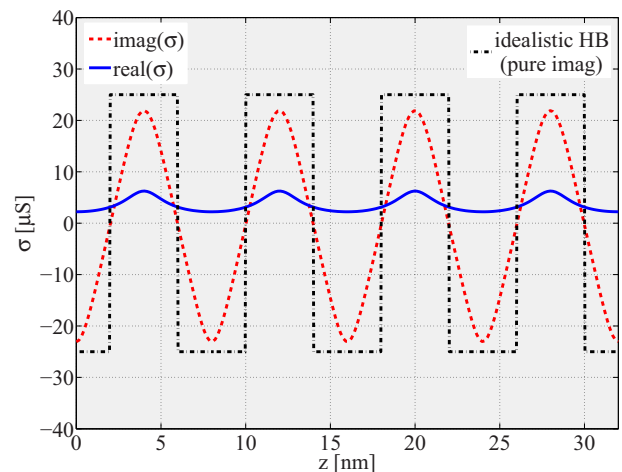


FIG. 3. (Color online) The conductivity distributions resulting from the bias modulation scheme depicted in Fig. 2 for $f = 10$ THz, $T = 3$ K, and $\Gamma = 0.215$ meV. Also shown is the idealized hard-boundary case discussed in Ref. [50].

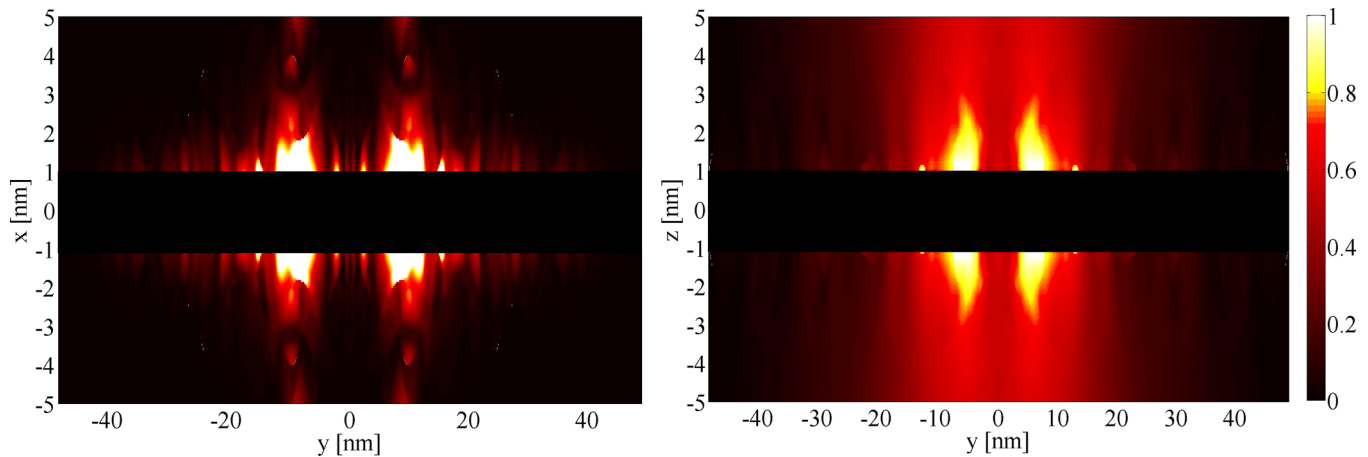


FIG. 4. (Color online) The normalized x component of the electric field at the source (left) and image (right) planes (same color scale) of the modulated graphene surface in the lossless case. Source and image lines are at separated by $2\lambda_{\text{SPP}}$ (the region $-1 < x < 1$ is the dielectric slab model of graphene).

or chemical doping), its effective anisotropic conductivity can indeed satisfy (3).

In the following, two conductivity modulations will be analyzed whose effective anisotropic conductivities satisfy (3) and are thus in principle capable of canalizing SPPs. Since we will use full-wave simulations to confirm the canalization geometries, a section in [50] is dedicated to modeling of graphene in commercial simulation codes using finite-thickness dielectrics.

III. MODULATED CONDUCTIVITY USING RIDGED GROUND PLANES

In previous canalization metamaterials, or hyperlenses, using alternating positive and negative dielectrics, an idealized, abrupt transition has been assumed between layers. For graphene, this would be analogous to strips having abrupt transitions between positive and negative imaginary-part conductivities. We refer to this as the hard-boundary case, and analyze it in detail in Ref. [50]. However, given the finite quantum capacitance of graphene, such an abrupt transition is impossible to achieve. A more realistic modulation scenario for a conductivity profile satisfying (3) can be obtained in the geometry of Fig. 2. It consists of an infinite sheet of graphene gated by a ridged ground plane, as shown in the insert of Fig. 2. Performing a static analysis, it is possible to obtain the charge density on the graphene layer, which may in turn provide

the chemical potential and the conductivity of graphene following a method analogous to Ref. [23]. Figure 3 shows the calculated conductivity of the graphene layer as a function of z for $f = 10$ THz, $T = 3$ K, and $\Gamma = 0.215$ meV (using the complex conductivity predicted by the Kubo formula; see Ref. [11] for the explicit expression); these parameters are used throughout.

Two important conclusions can be drawn from Fig. 3: (i) the imaginary part of conductivity dominates the real part, as desired, and (ii) its distribution is almost perfectly sinusoidal, which, after insertion into (5) and (6), satisfies (3). Therefore the geometry of Fig. 2 may be expected to support canalization. The resulting graphene nanoribbons have a realistic smooth variation in conductivity; we refer to this geometry as the soft-boundary scenario, considered in the following.

As an example, we first consider the lossless case $\sigma = -j\sigma^i$. Two point sources are placed in front of the source line in Fig. 1, exciting SPPs on the graphene layer. The point sources, which in our model are 1 nm long, x -directed electric dipoles, are separated by 20 nm $= 0.15\lambda_{\text{SPP}}$, where $\lambda_{\text{SPP}} = 133$ nm using (S.2) in Ref. [50], and the canalization area (the region between the source and the image lines) has length $2\lambda_{\text{SPP}} = 250$ nm and width of 100 nm (which is large compared to the separation between sources). The simulations shown here omit the biasing ground plane, since we found it to have minimal effect on the results, due to the transverse field concentration of the SPP around the graphene layer.

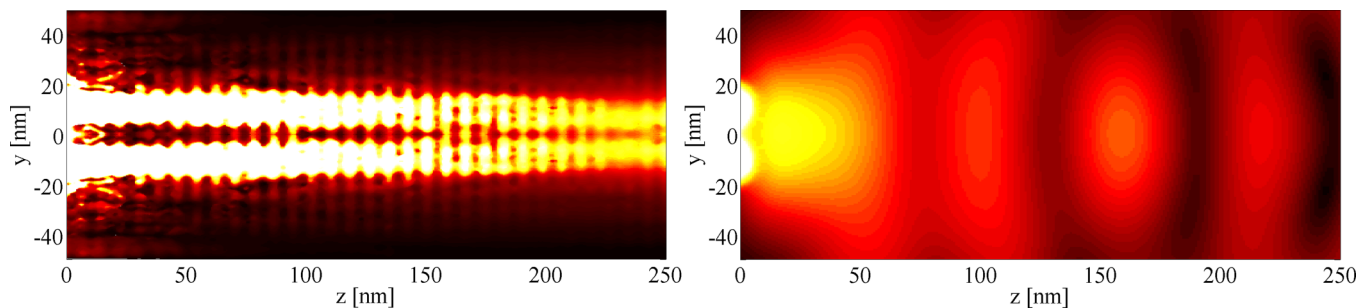


FIG. 5. (Color online) Normalized x component of the electric field above the modulated graphene surface (left) and a homogenous graphene surface (right). Color scale is the same as Fig. 4.

Figure 4 shows the x component of the electric field at the source line and image line (at the end of the modulated region). Figure 5 shows the x component of the electric field above the modulated graphene surface of Fig. 4, and a homogenous graphene surface with conductivity $\sigma = -j23.5 \mu\text{S}$ (corresponding to the maximum conductivity in Fig. 3). In both figures, the values are normalized to their own maximums. This shows quite strikingly how the canalization occurring on the modulated graphene can avoid the usual diffraction expected on a homogeneous layer. Figs. S.3–S.5 in Ref. [50] show corresponding results for the hard-boundary case.

We found that slightly changing the permittivities can result in converging or diverging beams. Here, we use integer values for the permittivities rather than specifying permittivity values to unrealistic levels of precision [50]. In an experiment, the best canalization point can be found by finely tuning the bias voltage.

It is easy to show that (5) and (6) cannot be exactly satisfied if the conductivity includes loss (i.e., the real part of σ). Therefore as loss increases, the phase velocities will differ among various spatial components and, as a result, one would expect to see a blurred image, and eventually no image, as loss further increases. To investigate this deterioration effect, we decrease the canalization length to $200 \text{ nm} = 1.5\lambda_{\text{SPP}}$ and increase the separation between sources to $50 \text{ nm} = 0.4\lambda_{\text{SPP}}$ (which we found necessary to maintain accuracy in the simulation). The geometry is then simulated for soft- and hard-boundary cases (with and without loss for each case) and the x components of the electric field at $x = 10 \text{ nm}$ are shown in Fig. 6. The curves are calculated in the image line at a distance 1 nm above the graphene surface.

Comparison between the four curves in Fig. 6 shows that the lossless hard- and soft-boundary examples yield similar results, as expected since their effective surface conductivities satisfy (3) exactly. In fact, as long as the period is small compared to the wavelength, any modulation that has half-wave symmetry will satisfy (3), leading to perfect canalization.

However, adding loss causes the effective surface conductivities to have nonvanishing real parts, and therefore (3) cannot be exactly satisfied. In the lossy case, the modulation scheme is important, since it affects how closely (3) can be achieved.

Image degradation due to loss can be lessened by working at higher frequencies. In fact, the maximum of the ratio $\text{Im}(\sigma)/\text{Re}(\sigma)$ may be increased by adjusting the chemical potential at higher frequencies. In Fig. S.8 of Ref. [50], the ratio $\text{Im}(\sigma)/\text{Re}(\sigma)$ is shown as a function of chemical potential and frequency. The simulation results confirm the improvement

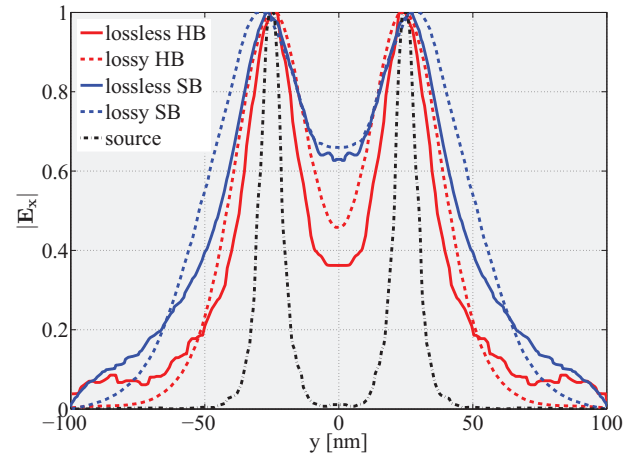


FIG. 6. (Color online) The effect of loss on the image canalization for hard- and soft-boundary bias modulations as shown in Fig. 3.

of canalization as frequency increases since the ratio $\text{Im}(\sigma)/\text{Re}(\sigma)$ increases with increasing frequency.

Our results show that a triangular ridged ground plane used to bias the graphene monolayer indeed allows canalization and hyperlensing, since its effective conductivities given by (5) and (6) satisfy (3). However, there are many possible $\sigma(z)$ functions that, after inserting them into (5) and (6), will satisfy (3). As an example, the sinusoidal conductivity of Fig. 3 can also be implemented using a rectangular ridged ground plane (details are shown in Ref. [50]).

IV. CONCLUSIONS AND FUTURE SCOPE

We have analyzed the possibility to produce in-plane canalization of SPPs on a 2D surface, with particular emphasis on its realization in a realistically modulated graphene monolayer, resulting in a planarized 2D hyperlens on graphene. We envision the use of this effect on a ridged ground plane for subwavelength imaging of THz sources and to arbitrarily tailor the front wave of an SPP by suitably designing the boundary of the canalization region.

V. METHODS

Simulations were performed with CST Microwave Studio [52] using a dielectric slab model of graphene, with the conductivity coming from the Kubo formula [15,16]. Reference [50] describes in detail the model, contains proofs of various equations appearing in the text, and presents additional results.

- [1] K. S. Novoselov, A. K. Geim, S. V. Morozov, D. Jiang, Y. Zhang, S. V. Dubonos, I. V. Grigorieva, and A. A. Firsov, *Science* **306**, 666 (2004).
- [2] A. H. Castro Neto, F. Guinea, N. M. R. Peres, K. S. Novoselov, and A. K. Geim, *Rev. Mod. Phys.* **81**, 109 (2009).
- [3] X. Luo, T. Qiu, W. Lu, and Z. Ni, *Mater. Sci. Eng., R* **74**, 351 (2013).

- [4] Y. Zhang, Y. W. Tan, H. L. Stormer, and P. Kim, *Nature (London)* **438**, 201 (2005).
- [5] L. A. Falkovsky and A. A. Varlamov, *Eur. Phys. J. B* **56**, 281 (2007).
- [6] L. A. Falkovsky and S. S. Pershoguba, *Phys. Rev. B* **76**, 153410 (2007).
- [7] S. A. Mikhailov and K. Ziegler, *Phys. Rev. Lett.* **99**, 016803 (2007).

- [8] V. P. Gusynin and S. G. Sharapov, *Phys. Rev. B* **73**, 245411 (2006).
- [9] V. P. Gusynin, S. G. Sharapov, and J. P. Carbotte, *Phys. Rev. Lett.* **96**, 256802 (2006).
- [10] N. M. R. Peres, A. H. Castro Neto, and F. Guinea, *Phys. Rev. B* **73**, 195411 (2006).
- [11] G. W. Hanson, *J. Appl. Phys.* **103**, 064302 (2008).
- [12] G. W. Hanson, *IEEE Trans. Antennas Propag.* **56**, 747 (2008).
- [13] N. M. R. Peres, F. Guinea, and A. H. Castro Neto, *Phys. Rev. B* **73**, 125411 (2006).
- [14] K. Ziegler, *Phys. Rev. B* **75**, 233407 (2007).
- [15] N. W. Ashcroft and N. D. Mermin, *Solid State Physics* (Saunders College Publishing, Philadelphia, 1976).
- [16] V. P. Gusynin, S. G. Sharapov, and J. P. Carbotte, *J. Phys.: Condens. Matter* **19**, 026222 (2007).
- [17] A. Vakil and N. Engheta, *Science* **332**, 1291 (2011).
- [18] J. Christensen, A. Manjavacas, S. Thongrattanasiri, F. H. L. Koppens, and F. J. G. de Abajo, *ACS Nano* **6**, 431 (2011).
- [19] G. W. Hanson, E. Forati, W. Linz, and A. B. Yakovlev, *Phys. Rev. B* **86**, 235440 (2012).
- [20] A. Yu. Nikitin, F. Guinea, F. J. García-Vidal, and L. Martín-Moreno, *Phys. Rev. B* **84**, 161407(R) (2011).
- [21] D. L. Sounas and C. Caloz, *Appl. Phys. Lett.* **98**, 021911 (2011).
- [22] W. Wang, P. Apell, and J. Kinaret, *Phys. Rev. B* **84**, 085423 (2011).
- [23] E. Forati and G. W. Hanson, *Appl. Phys. Lett.* **103**, 133104 (2013).
- [24] M. A. K. Othman, C. Guclu, and F. Capolino, *J. Nanophotonics* **7**, 073089 (2013).
- [25] M. A. K. Othman, C. Guclu, and F. Capolino, *Optics Express* **21**, 7614 (2013).
- [26] H. Raether, *Surface Plasmons* (Springer, Berlin, 1988).
- [27] A. Y. Nikitin, F. Guinea, F. J. Garcia-Vidal, and L. Martin-Moreno, *Phys. Rev. B* **84**, 195446 (2011).
- [28] C. Berger, Z. Song, X. Li, X. Wu, N. Brown, C. Naud, D. Mayou, T. Li, J. Hass, and A. N. Marchenkov, *Science* **312**, 1191 (2006).
- [29] T. Mueller, F. Xia, M. Freitag, J. Tsang, and P. Avouris, *Phys. Rev. B* **79**, 245430 (2009).
- [30] R. R. Nair, P. Blake, A. N. Grigorenko, K. S. Novoselov, T. J. Booth, T. Stauber, N. M. R. Peres, and A. K. Geim, *Science* **320**, 1308 (2008).
- [31] F. Bonaccorso, Z. Sun, T. Hasan, and A. C. Ferrari, *Nat. Photon.* **4**, 611 (2010).
- [32] F. N. Xia, T. Mueller, Y. M. Lin, A. Valdes-Garcia, and P. Avouris, *Nat. Nanotechnol.* **4**, 839 (2009).
- [33] K. F. Mak, M. Y. Sfeir, Y. Wu, C. H. Lui, J. A. Misewich, and T. F. Heinz, *Phys. Rev. Lett.* **101**, 196405 (2008).
- [34] T. Otsuji, S. B. Tombet, A. Satou, H. Fukidome, M. Suemitsu, E. Sano, V. Popov, M. Ryzhii, and V. Ryzhii, *J. Phys. D: Appl. Phys.* **45**, 303001 (2012).
- [35] C. Docherty and M. Johnston, *J. Infrared Millim. Terahertz Waves* **33**, 797 (2012).
- [36] J. S. Gmez-Daz, M. Esquiús-Morote, and J. Perruisseau-Carrier, *Opt. Express* **21**, 24856 (2013).
- [37] Y. Jiang, W. Lu, H. Xu, Z. Dong, and T. Cui, *Phys. Lett. A* **376**, 1468 (2012).
- [38] P. Y. Chen and A. Alù, *ACS Nano* **5**, 5855 (2011).
- [39] Y. Liu, X. Dong, and P. Chen, *Chem. Soc. Rev.* **41**, 2283 (2012).
- [40] S. Szunerits, N. Maalouli, E. Wijaya, J. Vilcot, and R. Boukherroub, *Anal. Bioanal. Chem.* **405**, 1435 (2013).
- [41] J. B. Pendry, *Phys. Rev. Lett.* **85**, 3966 (2000).
- [42] V. Veselago, *Sov. Phys. Usp.* **10**, 509 (1968).
- [43] P. Ikonen, P. A. Belov, C. R. Simovski, and S. I. Maslovski, *Phys. Rev. B* **73**, 073102 (2006).
- [44] E. E. Narimanov and V. M. Shalaev, *Nature (London)* **447**, 266 (2007).
- [45] A. Salandrino and N. Engheta, *Phys. Rev. B* **74**, 075103 (2006).
- [46] P. A. Belov and Y. Hao, *Phys. Rev. B* **73**, 113110 (2006).
- [47] P. A. Belov, Y. Zhao, S. Tse, P. Ikonen, M. G. Silveirinha, C. R. Simovski, S. Tretyakov, Y. Hao, and C. Parini, *Phys. Rev. B* **77**, 193108 (2008).
- [48] G. W. Hanson, A. B. Yakovlev, and A. Mafi, *J. Appl. Phys.* **110**, 114305 (2011).
- [49] P. A. Belov, C. R. Simovski, and P. Ikonen, *Phys. Rev. B* **71**, 193105 (2005).
- [50] See Supplemental Material at <http://link.aps.org/supplemental/10.1103/PhysRevB.89.081410> for the details of the model, proofs of various equations appearing in the text, and additional results.
- [51] S. A. Ramakrishna, J. B. Pendry, M. C. K. Wiltshire, and W. J. Stewart, *J. Mod. Opt.* **50**, 1419 (2003).
- [52] CST Microwave Studio, <http://www.cst.com>.